“Brittle structural facies” analysis: A diagnostic method to unravel and date multiple slip events of long-lived faults

"Brittle structural facies" analysis: A diagnostic method to unravel and date multiple slip events of long-lived faults

Giulia Tartaglia[a]*, Giulio Viola[a*], Roelant van der Lelij[b], Thomas Scheiber[c], Alberto Ceccato[a], Jasmin Schönenberger[b]

[a] Dipartimento di Scienze Biologiche, Geologiche ed Ambientali – BiGeA, Università degli studi di Bologna, Via Zamboni 67, 40126 Bologna, Italy

[b] Geological Survey of Norway, 7491 Trondheim, Norway

[c] Western Norway University of Applied Sciences, Department of Environmental Sciences, Sogndal, Norway

*Corresponding authors:
Giulia Tartaglia, giulia.tartaglia4@unibo.it Via Zamboni 67, 40126, Bologna, Italy
Giulio Viola, giulio.viola3@unibo.it Via Zamboni 67, 40126, Bologna, Italy

Giulia Tartaglia: giulia.tartaglia4@unibo.it
Giulio Viola: giulio.viola3@unibo.it
Roelant van der Lelij: roelant.vanderlelij@ngu.no
Thomas Scheiber: thomas.scheiber@hvl.no
Alberto Ceccato: alberto.ceccato@unibo.it
Jasmin Schönenberger: jasmin.schonenberger@ngu.no

Abstract

Large faults typically experience complex, long-lasting histories, commonly recording evidence of multiple reactivation events. Therefore, faults contain multiscalar structural domains characterised by varying microstructures, mineralogical compositions and kinematics. These domains result from differential strain partitioning during the recorded

faulting stages, and, as a result, can preserve the isotopic and kinematic signature of the different slip periods. Their detailed structural analysis integrated with K-Ar dating of the fault rock assemblage can help to identify these commonly tightly juxtaposed, although not coeval, domains, which we refer herein to as “Brittle Structural Facies” (BSF). BSF analysis is pivotal (i) to understand the structural heterogeneity of fault zones, (ii) the diachronic formation of geometrically and kinematically complex fault cores and (iii) to reconstruct faults’ evolution in time and through space. Following this approach, this study relies on meso- and microstructural analysis, chemical characterisation and K-Ar dating to unravel the evolution of the Lærdal-Gjende Fault (LGF, southwestern Norway). The LGF is a multiply reactivated top-to-the-NW extensional fault with a 1 m thick poorly consolidated core. We recognised, sampled and characterised five BSF: I) Indurated dark reddish gouge, (II) Poorly consolidated cataclasite, (III) Weakly foliated greenish gouge, (IV) Clay-rich gouge and (V) A few mm-thick clay smear decorating the principal slip surface. Samples were separated into five grain size fractions (from <0.1 to 6-10 μm) and analysed by X-Ray Diffraction, Transmission Electron Microscopy and K-Ar geochronology. A c. 180 Ma age cluster defined by 10 ages of the coarsest grain size fractions (2-10 μm) likely documents fault nucleation during Jurassic rifting in the North Sea. The ages of the finest fractions, enriched in synkinematic K-bearing minerals (illite, smectite and K-feldspar), constrain four periods of faulting at c. 121±3, 87±2, 78±2 and 57±1 Ma. Ages indicate that the LGF accommodated strain due to hyperextension of the Mid-Norwegian margin down to the Late Cretaceous and finally slipped again during the Paleogene. The alternating widening and narrowing of the active fault zone in response to varying deformation mechanisms, including coseismic rupturing, formed the present complex fault architecture. This study highlights the importance of BSF characterisation as part of a multidisciplinary workflow to derive structural and temporal datasets of complex fault zones. BSF analysis,

moreover, is demonstrated to be key for investigating the diachronic evolution of fault cores and to resolve multiple slip events of long-lived faults.

Keywords: Brittle deformation, Brittle Structural Facies (BSF), K-Ar fault rock dating, Strain localization**.**

1. Introduction and aims of the study

Fault zones are expression of brittle deformation in the Earth upper crust, where slip localises in response to stresses that exceed the rock strength. Their nucleation and progressive growth lead to the formation of fault cores and surrounding damage zones (Chester and Logan, 1986; Caine et al., 1996). Different fault-related rocks, such as cataclasite, breccia, gouge and pseudotachylyte, may commonly coexist within the same fault zone. Their juxtaposition reflects the temporal and spatial evolution of the fault system, including its deformation mechanisms and physical conditions at the time of initial faulting, as well as of possible reactivations.

Many brittle faults can be interpreted as the summation of multiple deformation events through time. During each faulting episode, slip and strain localisation lead to progressive comminution of the host rock and synkinematic crystallisation of new minerals, such as clays and phyllosilicates. Importantly, *in situ* synkinematic neoblastesis offers the possibility to radiometrically date a given faulting event as well as later multiple reactivations (e.g. van der Pluijm et al., 2001; Pleuger et al., 2012; Bense et al., 2013; Davids et al., 2013; Yamasaki et al., 2013; Torgersen et al., 2015a; Ksienzyk et al., 2016; Viola et al., 2016, 2018; Aldega et al., 2019; Scheiber et al., 2019).

Unravelling the relationships between mineral assemblages, age and kinematic framework of all recorded slip events within a fault remains an arduous task (Clauer, 2013; Torgersen et al., 2015a; Viola et al., 2016; Scheiber et al., 2019). The intrinsic complexity of faults

and the spatial arrangement of fault rocks reflect the interplay of fluid-rock interaction and the ease of reactivation of brittle structures. The reactivation of suitably oriented faults (Holdsworth, 2004) may lead to the partial or total obliteration of any inherited evidence of earlier deformation events (Viola et al., 2013). Due to these complexities, conceptual evolutionary models of fault zones do not always consider the absolute temporal dimension of faulting, and thus become rather static snapshots of what is instead a dynamic evolution. The lack of details on the temporal dimension of faulting may lead to oversimplifications of the evolution of faults, which, in turn, can lead to a misinterpretation of their possible seismic behaviour and overall tectonic role in the regional framework.

The necessity of a time-constrained reconstruction of faults' evolution has therefore led structural geologists to study in detail their internal architecture (e.g. Caine et al., 1996; Aydin, 2000), which often contains juxtaposed domains characterised by different fault rocks, mineralogical composition, texture and kinematics. Multiple faulting events cause deformation to preferentially localise into weaker volumes and along slip surfaces, whereas lithons representing remnants of former slip events can be preserved. These domains generally exhibit sharp boundaries and complex crosscutting relationships whose unravelling is crucial to establish a relative temporal sequence of (de)formation. We apply inhere the term "Brittle Structural Facies" (BSF) to refer to such domains (cf. Braathen et al., 2009). In this paper, BSF specifically refers to a deformed volume of rock characterised by a given fault rock type, texture, colour, composition, and age of formation. The identification, structural analysis, mineralogical characterisation and radiometric dating of BSF are key to (i) understand the structural heterogeneity of fault zones, (ii) decipher the diachronic formation of geometrically and kinematically complex fault cores and (iii) resolve the evolution of multiply reactivated faults.

To document our approach and the usefulness of the BSF concept, we present a structural-geochronological workflow that serves as an example of general validity when aiming to unravel the evolution of long-lived faults. We studied the Lærdal-Gjende Fault (LGF), a multiply reactivated extensional fault in southwestern Norway (Andersen et al., 1999; Fossen and Hurich, 2005; Fossen et al., 2016). The detailed structural analysis of the fault core allowed us to identify five distinct BSF, and to sort out their mutual geometric and relative temporal relationships. Samples from each brittle fault facies were characterised by optical and Scanning Electron Microscopy (SEM). K-bearing phases from fault rock samples were identified, quantified and characterised by X-Ray Diffraction (XRD) and Transmission Electron Microscopy (TEM) and, finally, dated by the K-Ar technique. This comprehensive structural, compositional and geochronological dataset has been used to propose an evolutionary scheme of LGF that accounts for all dated faulting stages.

2. Geological framework

The study area is in southwestern Norway, near the town of Lærdal (Fig. 1a). There, the Baltic autochthonous basement is overlain by Caledonian Allochthons (Corfu et al., 2014) thrusted south-eastward during the Late Silurian-Early Devonian Caledonian collision between Baltica and Laurentia (Fossen and Dunlap, 1998). The autochthonous basement is mainly composed of Mesoproterozoic migmatites that were only marginally affected by Caledonian deformation (Fossen and Hurich, 2005). The Allochthons are tectonic nappes derived from the cover sequences of the Baltic Shield, the ancient Iapetus Ocean and Laurentian basement cover units. The allochthonous unit at the Lærdal site is formed by the Laurentia-derived Jotun Nappe Complex. It is composed of a series of thrust sheets of variously deformed plutonic rocks metamorphosed under amphibolite facies conditions during the Proterozoic Sveconorwegian orogeny (Milnes and Corfu, 2011; Corfu et al.,

2014). The Jotun Nappe Complex comprises monzonitic and mangeritic orthogneiss, metagabbroic slivers and anorthositic suites (Milnes and Corfu, 2011).

Caledonian collisional tectonics led to an over-thickened orogenic pile that collapsed during the Early Devonian (408-402 Ma; Fossen and Dunlap, 1998) through the nucleation and reactivation of orogen-scale extensional detachments. NW-SE extension caused the exhumation of the orogenic roots to shallow crustal levels. The progressive accommodation of deformation in the brittle regime led to the nucleation of major faults and brittle fault zones, which overprinted earlier ductile detachments (Fossen et al., 2016). One of these Devonian extensional detachments is the Hardangerfjord Shear Zone (HSZ), which is exposed in the study area (Fig. 1a, Fossen et al., 2016). The HSZ is a gently oblique top-to-the-NW shear zone (Fossen and Hurich, 2005), which is composed at the Lærdal site of tens of meter thick mylonites separating the autochthonous basement from the overlying Jotun Nappe Complex (Fig. 1a). The Lærdal-Gjende Fault strikes NE-SW, and at its most representative outcrop in Lærdal it partially reworked and overprinted the mylonitic fabric of the HSZ (Fig. 1a, Fossen and Hurich, 2005).

Thermochronological studies indicate that two main episodes of enhanced, rapid exhumation affected southwestern Norway in the Permo-Triassic and in the late Cretaceous-Cenozoic (Johannessen et al., 2013; Walsh et al., 2013; Ksienzyk et al., 2014, 2016). During the Cretaceous, exhumation generated a high relief that was later periodically rejuvenated by brittle faulting (Johannessen et al., 2013).

Two studies have focused on the age of brittle deformation along the LGF. Andersen et al. (1999) studied the greenish epidote-rich cataclasite in the damage zone and constrained Early Triassic up to Early Cretaceous slip by paleomagnetic techniques. Fossen et al. (2016) used K-Ar radiometric dating on synkinematic illite from two fault core gouge samples reporting dates between 200 and 64 Ma. In general, previous authors agree that

the LGF nucleated and developed as the shallow crustal brittle expression of the ductile HSZ during the Devonian (although direct geochronological constraints on this episode are not reported), and continued its activity until the Cretaceous, to around 120 Ma. Hence, according to published data, the LGF was active during the post-collisional collapse of the Caledonides and during the Mesozoic North Sea rifting evolution (Andersen et al., 1999; Fossen and Hurich, 2005; Fossen et al., 2016). These studies, however, did not aim at linking the different fault structural facies to their ages, and a time-constrained evolutionary model of the LGF has not yet been proposed.

3. Methods

Our study is based on a combined structural-geochronological approach (Viola et al., 2016) wherein a detailed structural analysis of the fault was done by identifying, describing and characterising different BSF. Characterisation of the BSF and structural analysis were performed along the entire LGF outcrop exposed in Lærdal (Fig. 1). Sample collection was from the central part of the LGF outcrop, in a well exposed c. 1 m^2 portion of the fault core (Fig. 1c). C. 400 g of variably consolidated fault rock material was collected for each BSF (Fig. 1d). Special care was taken to avoid mixing between different BSF. Oriented samples of consolidated fault rock and wall rock were collected for microstructural analysis. Thin sections oriented parallel to the transport direction and perpendicular to the planar fabric were prepared from the poorly consolidated samples of cataclasite and indurated gouge. They were studied by optical and scanning electron microscopy equipped with an energy dispersive X-ray analyser (SEM-EDS) at the University of Padua (Italy) to investigate microstructure and mineralogical composition of the fault rocks.

Characterisation of the samples for K-Ar radiometric dating was performed at the laboratories of the Geological Survey of Norway (Trondheim, Norway) following the routines described by Viola et al. (2018). Samples from each BSF were disintegrated by

repeated freezing and thawing cycles. This method avoids artificial grain size reduction of coarse-grained minerals and their contamination in the finer fractions. Samples were separated in five grain size fractions (<0.1, 0.1-0.4, 0.4-2, 2-6 and 6-10 μm). Grain size fractions of <2, 2-6 and 6-10 μm were separated in distilled water using Stokes' law, whereas the finer fractions (<0.1, 0.1-0.4 and 0.4-2 μm) were obtained by high speed centrifugation of the <2 μm fraction.

The mineralogical composition of each grain size fraction for each sample was obtained by XRD analysis (with a Bruker D8 Advance diffractometer). Mineral quantification was carried out on randomly prepared specimens using Rietveld modelling with the TOPAS 5 software. Refined parameters include crystallite size, unit cell dimensions, sample displacement, preferred orientation and background coefficients. The lower limit of quantification and accuracy are mineral-dependent but are generally 1 wt% and 2-3 wt%, respectively. The finest <0.1 μm grain size fractions could not be analysed by XRD due to too low sample mass being recovered from these fractions. Detection and imaging of K-bearing phases therein were thus carried out with a TEM (JEOL JEM-2100) equipped with an energy dispersive X-ray analyser (EDS) at the NORTEM laboratory of the Norwegian University of Science and Technology. After the structural characterisation of the BFS, and the identification of the K-bearing phases, all grain size fractions were dated by K-Ar technique. Readers are referred to Appendix for further details on the analytical procedure.

4. Results

4.1 Fault anatomy and sample location

The LGF is a composite brittle structure defined by a 1-1.5 m thick fault core and an up to 200 m thick asymmetric damage zone. The damage zone is mainly composed of grey-pale green cohesive cataclasite and is thicker in the hanging wall. A dense and complex network of 1-3 cm thick epidote and quartz veins cuts across the hanging wall (Fig. 2a),

but is not present in the immediate proximity of- and within the fault core. Towards the upper part of the hanging wall, metasyenite and metamonzogranite are exposed. In the footwall mylonites, the damage zone is up to 30 m thick.

The fault core is a tabular structure containing a principal slip surface that dips 35° to the NW and bears W-plunging slickenlines (Fig. 1b). It is defined by a laterally continuous and only a few mm thick smear of dark gouge (Fig. 1d). Secondary slip surfaces, subparallel to the principal slip surface, occur above and below it, bounding the fault core (Figs. 1b, c). They contain two sets of lineations, defined by NW- and W- plunging slickenlines (Figs. 1b, 2b). Riedel shears and bookshelf structures (Figs. 2e, f), together with the bending of foliated gouge and sigmoidal lenses of indurated cataclasite (Figs. 2c, d), are consistent with a normal top-to-the-NW sense of shear. The principal slip surface cuts across all other structural features (Fig. 1d), indicating that its sinistral transtensional W-directed kinematics is related to the youngest recorded increment of faulting.

The fault core contains juxtaposed discrete brittle domains delimited by sharp boundaries, each corresponding to one of the identified BSF of the LGF (Fig. 1d). Every BSF contains a distinct fault rock type, each characterised by a different degree of consolidation, colour, clay content (with various degrees of plasticity in hand specimen) and geometric relationships. Five BSF (BSF I to BSF V) were recognised at the outcrop (Fig. 1d) and sampled for mineralogical characterisation and K-Ar dating.

Crosscutting relationships at the outcrop allowed to define the relative temporal sequence of BSF formation, from the oldest (BSF I) to the youngest (BSF V). The fault core contains competent and internally fractured lenses of a dark reddish grey indurated gouge (BSF I, Fig. 3a) preserved all along a tabular domain in the central portion of the core. These lenses are a few to tens of cm long and locally exhibit sigmoidal shapes (Fig. 2d). They are embedded within two other brittle structural facies: a poorly consolidated cataclasite (BSF

II) and a weakly foliated gouge (BSF III, Fig. 1d). BSF II defines the most external portion of the core and is formed by a poorly consolidated pale green cataclasite (Fig. 3b). It is the most abundant structural facies in the fault core. Inside the green cataclasite there occur smaller sigmoidal lenses of whitish cataclasite (identical in thin section to the greenish cataclasite of BSF II), whose asymmetric shape suggests top-to-the-NW extensional shearing (Figs. 1d, 2c). The green cataclasite is cut across by narrowly spaced, subvertical, NNE-SSW striking fractures with sporadic calcite coatings. These subvertical fractures are found exclusively within this cataclastic BSF and do not crosscut the younger gouges (BSF III, IV and V). The fine-grained, weakly foliated greenish gouge (BSF III, Fig. 3c) cuts the green cataclasite (BSF II) and the associated system of fractures.

White, undulating zeolite veins are sub-parallel to the principal slip surface (Fig. 2f). These veins are spatially associated with the dark reddish grey gouge (BSF I), cutting the lenses thereof and the weakly foliated gouge around it (BSF III). Both lenses and veins are, in turn, crosscut by sub-vertical fractures, whose geometrical arrangement is consistent with top-to-the-NW extensional shearing.

Two other distinct types of clay-rich gouge occur in the inner part of the core. A green-grey and plastic gouge variety is preserved exclusively at the north-western exposed termination of the fault, geometrically below the principal slip surface (BSF IV, Fig. 3d). Finally, the BSF V is represented by the smear of dark, clay-rich gouge along the principal slip surface (Fig. 3e), which forms a laterally continuous 2-3 mm-thick layer and cuts all the BSF described above (Fig. 3f).

4.2 Microstructural analysis

The damage zone in the hanging wall is mainly composed of proto-cataclastic to ultracataclastic rocks (Fig. 4b). They are formed at the expense of a mylonitic gneiss (Fig.

4a) made of quartz-feldspar ribbons wrapped around by chlorite and epidote-rich layers along the foliation (Figs. 4a, b). Quartz grains in the mylonitic domains are a few to tens of μm in size, have lobate boundaries and diffuse undulose extinction. Feldspars are commonly altered to sericite. Relict nuclei of K-feldspar with exsolution lamellae occur in the centre of sigmoidal lithons, embedded within the foliation (Fig. 4a). An early generation of coarse epidote is overprinted by a subsequent finer-grained generation. The evidence of brittle deformation intensifies toward the core as documented by increased fracture density and the occurrence of discrete gouge levels composed of fine-grained epidote, clay and opaque minerals (Fig. 4b).

Rocks in the fault core form a heterogeneous fault rock assemblage from a microstructural point of view. The dark reddish grey indurated gouge (BSF I) is mainly composed of ultrafine-grained feldspar and clay minerals. Additionally, it exhibits rounded glassy and microcrystalline domains, containing spherulites varying in diameter from 5 to 10 μm (Fig. 4c). Consistent with the common interpretation of spherulites as diagnostic textures of frictional melts (e.g., Lin, 1994, Di Toro and Pennacchioni, 2004), we interpret these domains as heavily reworked and transposed clasts of pseudotachylyte veins, now preserved in the reddish gouge (BSF I).

The pale green cataclasite (BSF II), which forms the thickest portion of the LGF core, is composed of different domains and types of clasts (Figs. 4d, e). These clasts are embedded within an ultracataclastic and locally weakly foliated matrix (Fig. 4e) consisting of plagioclase, quartz, epidote, smectite and titanite. All clasts are invariably cut by Fe-chlorite and K-feldspar veins (Fig. 4f), themselves transposed and reworked in the ultracataclastic matrix. Some clasts are foliated and made of tightly spaced bands enriched in quartz and feldspars alternated with epidote-rich layers (Fig. 4d). The foliation

in these clasts and the evidence of crystal-plastic deformation suggest that they are derived from the host rock mylonite.

Other clasts within the pale green cataclasite are, instead, remnants of earlier generations of brittle fault rocks. Dark reddish, very fine-grained clasts are interpreted to be derived from BSF I. Some clasts in the pale green cataclasite, moreover, contain a fine-grained matrix embedding variably sized, reworked sub-rounded quartz and plagioclase (Figs. 4d, f). Tiny K-feldspars, smectite, smectite-illite, plagioclase, apatite, quartz, oxides and Fe-sulphides form the matrix (Figs. 4d, f).

1 to 5 mm-thick zeolite veins cut across the fault core (BSF I, II and III) but are absent in the gouges along the principal slip surface. Zeolite forms either euhedral or stretched fibres elongated perpendicular or at high angle to the vein walls. Randomly oriented laumontite crystals are found in dilatant domains around angular clasts of earlier generations of fault rocks (Fig. 4g).

Vertical and sub-vertical calcite veins strike NE-SW and have a variable thickness between 10 μm and a few mm. Fibrous calcite crystals are oriented WSW-ENE/W-E, at high angle to the vein boundaries (Fig. 4h). In some veins, they exhibit tabular, thin twins (type I), indicating deformation temperatures <200 °C (Ferrill et al., 2004). A second episode of calcite crystallisation occurred after the formation of the zeolite veins, i.e., after the formation of the weakly foliated gouge (BSF III), and before the last slip event along the principal slip surface.

In summary, microstructural observations constrain an increasing intensity of brittle deformation toward the LGF core. Mylonite- and different generations of reworked cataclasite/gouge clasts indicate a polyphase deformation history. Clasts of

pseudotachylyte reworked within the indurated fault gouge prove the coseismic character of at least one of the early deformation events.

Microstructural analysis and the observed crosscutting relationships permit constraining the following temporal sequence of veining, from old to young: 1) Pervasive chaotic system of epidote and quartz veins within the damage zone (Fig. 2a). Fault rocks of the LGF core contain fractured and transposed lenses of these epidote-rich domains.; 2) Chlorite and feldspar-rich veins cutting across an early generation of fault gouge, now only preserved as clasts in the fault core rocks (Fig. 4f); 3) Calcite and zeolite veins not affecting the youngest generations of unconsolidated clay-rich gouge (BSF IV and V), and thus predating the last stages of LGF slip (see below).

4.3 Fault rock compositional data

Samples from all the studied BSF have different mineralogical compositions. The relative abundance of mineral phases varies with grain size within the same sample. K-feldspar, epidote, chlorite and smectite occur in all structural facies (Table 1). XRD analysis documents a gradual increase of clay minerals towards the finest fractions from a minimum of 4 to a maximum of 44 wt% in the 0.1-0.4 μm fractions (e.g., in BSF V the concentration of clay minerals quadruples, Fig. 5e). The most abundant clay minerals in the fault core are smectite and illite. TEM analysis confirms the presence of K-bearing phases also in the finest fractions where we could not carry out XRD analysis due to the lack of sufficient material. Illite, mostly Fe-illite, smectite and K-smectite were detected in <0.1 μm grain size fraction (Figs. 5a-c). K-feldspar is an additional K-bearing phase that is present in all grain size fractions of all samples. At the TEM, euhedral K-feldspar crystals have been documented to also occur in the <0.1 μm fraction of BSF I to IV (Fig. 5d). XRD and TEM analysis do not document illite in any grain size fractions of BSF III, which, instead, contains smectite and K-feldspar.

In all samples, except that from BSF II, the percentage of K-feldspar decreases towards the finer grain size fractions (Fig. 5). In BSF I, K-feldspar ranges between 50 wt% in the coarser- and 30 wt% in the 0.1-0.4 μm grain size fraction. Similarly, the most clay-rich gouges (BSF IV and V) contain relatively high amounts of K-feldspar, which is still between 27 and 22 wt% in the finest fractions (Fig. 5e).

Chlorite is present in all dated fractions and its content tends to increase with decreasing grain size. Plagioclase is not ubiquitous in the samples, but it is one of the main components in BSF II and III. Epidote is a common phase in all BSF, but its content generally decreases with decreasing grain size. It is very abundant (c. 45 wt%) in the foliated greenish gouge of BSF III. Quartz is only sporadically found in BSF III, IV and V, and its concentration decreases steadily with grain size. Two zeolite types occur with different relative abundance, stilbite and laumontite (Table 1). Pyroxene does not exceed 6% and it is absent in BSF IV and V. Calcite occurs as an accessory phase.

In summary, the general trend of decreasing quartz, epidote and K-feldspar contents in the finer grain-size fractions (0.1-0.4 and 0.4-2 μm) is compensated by the increase of illite, smectite and chlorite. This trend suggests that quartz and epidote are protolithic minerals that did not crystallise during deformation. Pyroxene is a high temperature phase, and is thus considered to be inherited in all BSF. The euhedral habit of K-feldspar in the <0.1 μm grain size fraction (Fig. 5d), however, allows us to deduce that K-feldspar also grew authigenically during faulting. Moreover, the presence of zeolites in BSF I, II and III, which correspond to the most competent rocks in the fault core, allows us to constrain a maximum deformation temperature during faulting of c. 200 °C (Weisenberger and Bucher, 2010). At that temperature, K-feldspar is indeed capable to grow authigenically and sinkinematically (Mark et al., 2008; Sasseville et al., 2008; Brockamp and Clauer, 2013).

4.4 K-Ar radiometric data

K-Ar ages range from 195 ± 4 Ma to 57 ± 1 Ma (Table 2). “Radiometrically determined age vs. grain size” plots of the dated samples define inclined curves (Fig. 6), where the finest grain size fractions yield invariably the youngest ages, and the coarsest fractions (2-6, 6-10 μm) yield the oldest. All the ten ages of the 2-6 and 6-10 μm fractions define a cluster with a mean age of 179 ± 2 Ma (MSWD=7.4). The ages of the <0.1 μm fraction are 121 ± 3, 87 ± 2, 78 ± 2 Ma, and 57 ± 1 Ma. BSF I yielded the oldest <0.1 μm K-Ar age of 121 ± 3 Ma; its coarsest grain size fraction (6-10 μm) yielded an age of 186 ± 4 Ma. The weakly foliated gouge yielded dates between 87 ± 2 Ma for the <0.1 μm fraction, and of 167 ± 3 Ma for the 6-10 μm. The greenish clay-rich gouge, yielded dates between 78 ± 2 Ma and 184 ± 4 Ma for the <0.1 and 6-10 μm fractions, respectively. In BSF V, the <0.1 μm fraction yielded the youngest age of the entire dataset at 57 ± 1 Ma.

For the greenish cataclasite (BSF II) we could not date the <0.1 μm fraction; the 0.1-0.4 μm fraction yielded a date of 132 ± 3 Ma, which progressively increases towards the 6-10 μm fraction and represents the oldest age of the entire dataset at 195 ± 4 Ma. In the “age vs. grain size fraction” diagram of Fig. 6 the pale green line referring to BSF II can be traced between 121 and 87 Ma for the finest grain size. This age extrapolation does not follow any analytical constraints. The meso- and microstructural data from BSF II and the crosscutting relationships with the other structural facies allow us to conclude that the pale green cataclasite could be of Late Cretaceous age, i.e., an age between the formation of the reddish indurated- (BSF I) and of the weakly foliated gouge (BSF III).

5. Discussion

5.1 Interpretations of the new K-Ar dates

The “age vs. grain size” curves obtained during this study (Fig. 6) are conceptually identical to those produced by other K-Ar geochronological studies of fault-related rocks (Pevear, 1999; Zwingmann and Mancktelow, 2004; Bense et al., 2013; Davids et al., 2013;

Yamasaki et al., 2013; Torgersen et al., 2015a; Viola et al., 2016; Aldega et al., 2019). Such inclined curves are generally interpreted as recording variable contamination of the authigenic and synkinematic mineral phase separates by inherited protolithic minerals, mixing of different generations of authigenic minerals, and grain-size-dependent ^{40}Ar loss (van der Pluijm et al., 2001; Verdel et al., 2012; Torgersen et al., 2015a, b; Viola et al., 2016, Vrolijk et al., 2018).

Since brittle faulting is dilatational and may thus enhance the ingress of fluids into the actively deforming rock volume, synkinematic formation of new phases and/or recrystallisation of pre-existing minerals (or parts thereof) is common (Haines and van der Pluijm, 2008; Tagami, 2012; Vrolijk et al., 2018). Newly crystallised minerals will be the most abundant in the finer grain size fractions. Even the finest grain size fractions, however, may still include inherited protolithic minerals or different generations of authigenic phases reworked during multiple stages of deformation. Ages obtained from the finest grain size fractions should thus be still considered as maximum ages, although they provide the best available constraint on the timing of the most recent faulting event the rock recorded (van der Pluijm et al., 2001; Zwingmann and Mancktelow, 2004; Torgersen et al., 2015b; Viola et al., 2016).

The coarser grain size fractions, on the contrary, are enriched in protolithic (inherited) minerals, such as, for example, older generations of K-feldspar. If the coarser grain sizes of different samples from one single fault zone yield the same age, it is reasonable to conclude that they constrain a common thermal or faulting event. Such an early event likely occurred at higher temperature than the more recent ones recorded by the finer fractions (e.g., Viola et al., 2016; Vrolijk et al., 2018; Scheiber et al., 2019). The intermediate grain size fractions (0.4-2 and 2-6 μm) generally define a trend of decreasing age with decreasing grain size, as they result from the mixing of different (synkinematic

and protolithic) grains with varying isotopic signatures and are, therefore, commonly devoid of a real geological meaning.

In agreement with our compositional data, we adopt the Age Attractor Model (Torgersen et al., 2015a, b; Viola et al., 2016) and thus rely on the concept of progressively increasing amounts of authigenic and synkinematic K-bearing phases with decreasing grain size, such that we consider the finest fractions as mainly composed of authigenic, synkinematic minerals.

In this study, the ages of all BSF of the fault core span the c. 195 to 57 Ma time interval. Interestingly, there are no ages older than 195 ± 4 Ma (Jurassic). The Jurassic mean age of 179 ± 2 Ma calculated from all the 2-6 and 6-10 μm grain size fractions cannot be related to the age of the host rock, because the youngest host rock in Lærdal is Cambrian (Milnes and Corfu, 2011; Corfu et al., 2014). The c. 180 Ma age might, therefore, be interpreted as resulting from a major deformation event and be related to the initiation of brittle faulting along the LGF. The Jurassic and Early Cretaceous activity of the LGF was already constrained by previous authors by different dating techniques (Andersen et al., 1999; Fossen et al., 2016). Our obtained range of ages is comparable with results of Fossen et al. (2016), who documented ages between 191 and 64 Ma for the 2-6 μm and <0.2 μm fractions from the fault core of the LGF. From the common Jurassic age cluster of Fig. 6, each dated BSF follows a different “age vs. grain size” path. Post-Jurassic deformation and/or fluid ingress did thus not cause pervasive illite recrystallisation up to the coarsest fractions, which still yield their original Jurassic age, but instead synkinematic growth of illite up to the <2 μm grain size fractions. These results document therefore the evolution of rocks, which, from a single initial radiometric signature recorded at higher temperature, responded differentially during several later episodes of deformation. In fact,

each BSF tracks one of the subsequent deformation events with their specific compositional, structural and isotopic signatures (see Viola et al., 2016, their Fig. 5).

The K-Ar dating approach to brittle faults is generally applied on clays separated from fault rocks (van der Pluijm et al., 2001; Zwingmann and Mancktelow, 2004; Tagami, 2012; Vrolijk et al., 2018). TEM analysis is crucial to identify all K-bearing phases present in the finest fractions, such as illite, smectite and K-feldspar as they could either be simply inherited from the host rock and isotopically reset during faulting or be of authigenic, synkinematic origin (Mark et al., 2008; Sasseville et al., 2008; Surace et al., 2011; Torgersen et al., 2015b). Microstructural, compositional, and thermochronological data from the LGF suggest that the temperature did not exceed 200 °C during the Cretaceous (Ferrill et al., 2004; Weisenberger and Bucher, 2010; Johannessen et al., 2013). The Ar closure temperature for 1 μm illite/muscovite and K-feldspar grains is generally c. 210-250°C (Kelley, 2002; Verdel et al., 2012; Torgersen et al., 2015a). Thus, thermally induced volume diffusion effects, which could have reset the isotopic clock of the finest grain size fractions, are not considered in our interpretative model. Moreover, TEM images document the presence of authigenic Late Cretaceous K-feldspar, proving that it is indeed a synkinematic phase in the finest grain size fractions (see Torgersen et al., 2015a).

5.2 Fault evolution

In order to reconstruct the LGF evolution, being able to assign a K-Ar date to each recognised BSF allows us to correlate the age of K-bearing mineral authigenesis with a specific brittle deformation event. Microstructural observations indicate that the LGF grew in response to widespread cataclastic flow and fracturing superposed on an earlier ductile precursor. The presence of mylonite clasts and multiple generations of cataclasite/gouge support the interpretation of a polyphase deformation history. Additionally, the different

composition of each BSF suggests that the LGF has deformed different lithologies and units during its multiple reactivations.

In the following, we deconvolve the LGF deformation history and propose a time-constrained conceptual model for the fault (Fig. 7). The brittle fault partially reworked a precursor ductile shear zone (Fig. 7a). Deformation was likely associated with diffuse seismicity, generating pseudotachylytes. Crustal-scale extension caused the exhumation of deep crustal blocks and their progressive transition, while en-route to the surface, to colder and shallower conditions. Syndeformational fluid circulation created a pervasive network of epidote and quartz veins cutting through the mylonites and the proto-cataclasite that, by then, had formed mainly at the expense of the hanging wall sequence (Fig. 7a). Cross-cutting relationships visible at the outcrop permit to conclude that the c. 121 Ma old dark reddish grey and indurated gouge (BSF I) represents the oldest BSF preserved in the fault core. Its composition, with up to 50% K-feldspar in the coarsest grain size fraction, suggests that it formed at the expense of a K-feldspar-rich rock. Deformation and the ingress of fluid allowed the crystallisation of a clay-rich gouge with smectite, illite and chlorite, also embedding clasts of reworked pseudotachylyte (Fig. 7b). The remarkable hardness of the preserved lenses of this gouge, compared to the surrounding parts of the fault core, could be due to early induration processes by, for example, zeolite crystallisation (Table 1, Fig. 4g, Olsen et al., 1998). The early induration likely induced mechanical hardening of the fault core, requiring further deformation to affect a progressively wider volume of the rock by propagating into the hanging wall and footwall mylonites (Fig. 7c). A renewed episode of deformation formed the pale green cataclasite (BSF II), composed of heterogeneous clasts of older fault rocks (Fig. 7c). The finest grain size fraction (<0.1 μm) of the pale green cataclasite contained insufficient material for K-Ar analysis, but relative chronological constraints at the outcrop and microstructural evidence suggest that this BSF formed in the Late Cretaceous (Fig. 6, see Section 4.4). This BSF is

cut by NNE-SSW striking fractures, locally filled with calcite. The orientation of these fractures and veins constrain WNW-ESE extension, which is in agreement with the dominant normal kinematics of the fault. These fractures do not crosscut the younger gouges (BSF III, IV and V), indicating that BSF III to V post-date fracturing and the associated early calcite veining.

At c. 87 Ma a weakly foliated gouge formed in the centre of the fault core (BSF III, Fig. 7d). This Cretaceous and the following episodes of slip, up to the probable locking and healing of LGF at c. 57 Ma, were characterised by the narrowing of the active deformation zone. Fault narrowing was likely due to the progressive accumulation of clays in the core, and to the decreasing deformation temperature (Rutter et al., 2001; Scheiber et al., 2019). Slip was accommodated by the formation of a weakly foliated gouge and by the nucleation of Riedel shears in the consolidated fault facies (BSF I and II). BSF II and III contain plagioclase, K-feldspar and pyroxene, such that they probably derive from a mangeritic protolith of the Jotun Nappe Complex (Milnes and Corfu, 2011; Corfu et al., 2014). Interestingly, the foliated gouge of BSF III does not contain illite but smectite and K-feldspar. Almost identical amounts of K-feldspar are documented in all grain size fractions (c. 9-10%), because of its relative enrichment due to synkinematic neoblastesis.

In agreement with the discussed scenario of decreasing temperature through time, the progressive evolution of the fault caused the formation of unconsolidated, extremely localised fault gouges (BSF IV and V) in the centre of the core. BSF IV and V are distinctly different from the older brittle facies as they include significant amounts of smectite and illite. A green-grey gouge enriched in synkinematic illite, smectite and chlorite formed at 78 Ma (Fig. 7e). Finally, a thin, laterally continuous smear of dark gouge cut across all BSF, constraining a last transtensional top-to-the-W increment of faulting of the LGF at 57 Ma (Fig. 7f). The likely very low permeability of clay-rich gouge (Evans et al., 1997; Faulkner

and Rutter, 2003) suggests that crystallisation of illite and smectite occurred during faulting and not during post-deformational alteration. There is no evidence of other significant deformation episodes affecting the Paleogene clay-rich smear, and we conclude that the LGF ceased its (recorded) activity c. 57 Ma ago.

5.3 Regional implications

Our new dataset has also implications for the regional geological framework. The obtained LGF geochronological results do not record any evidence of fault activity prior to the Jurassic (Table 2), questioning whether this fault is indeed a Devonian structure (Corfu et al., 2014; Fossen et al., 2016). Lack of Palaeozoic ages in the studied BSF could be due to (1) selective sampling that would have missed potential pre-Jurassic domains, (2) Ar-loss or thermal effects or (3) obliteration of any pre-Jurassic isotopic signal in all grain size fractions. Our structural characterisation, however, was detailed and thorough and we sampled all BSF recognised at the main LGF outcrop. The LGF, however, is a very long brittle structure (Andersen et al., 1999) and we cannot exclude the possibility that Pre-Jurassic ages, if present, may be preserve elsewhere along the fault strike. Ar-loss or thermal effects can be considered unlikely in a system that underwent progressive cooling to below 250 °C from the Devonian onwards (Johannessen et al., 2013; Walsh et al., 2013; Ksienzyk et al., 2014, 2016 and references therein). As previous studies demonstrate, even in very highly-strained and multiply activated faults, earlier slip events are not completely obliterated, and they may be resolved by K-Ar dating of the coarser grain size fractions (Viola et al., 2016). As a consequence, Devonian to pre-Jurassic K-Ar ages, if ever present, would have most probably been preserved in the fault and detected during this study (cf. Torgersen et al, 2015). However, if the brittle LGF did accommodate a Palaeozoic history, it is likely that the structural and isotopic evidence thereof is

preserved only in the cohesive cataclasites and proto-cataclasites of the damage zone, which we did not date, and not in the fault core (e.g., Scheiber et al., 2019).

The LGF preserves evidence of at least five geological significant (re)activation episodes (from the Jurassic to the Paleogene), with indications of coseismic rupturing. Pseudotachylyte developed likely during the Jurassic or the possible earlier localisation history of the LGF. The oldest recorded event at c. 180 Ma could represent crustal stretching associated with the second phase of the North Sea rifting (Gabrielsen et al., 1999; Fossen et al., 2016; Viola et al., 2016). The Cretaceous events at c. 121, 87 and 78 Ma can be related to the hyperextension accommodation along the Mid-Norwegian margin during progressive cooling and exhumation (cf. Fossen et al., 2016; Ksienzyk et al., 2016; Scheiber and Viola, 2018). The last recorded Paleogene event (c. 57 Ma), documented by the laterally continuous clay smear along the principal slip surface, likely sealed the fault. The tectonic phase expressed by this geological feature remains, however, poorly constrained, even though other K-Ar Paleogene faulting ages are reported from southwestern Norway (Fossen et al., 2016; Scheiber et al., 2019).

6. Conclusion

We have presented a methodological approach that is of general validity and that can aid when reading geological archives stored in brittle faults. The present-day LGF core exposes the tight juxtaposition of several BSF. Each BSF is defined by specific fault rocks and is characterised by a unique isotopic signature, fully resolvable by K-Ar geochronology. This study also confirms that extreme localisation of strain, associated with synkinematic (re)crystallisation is indeed a common process within brittle faults (cf. Torgersen et al., 2015a; Viola et al., 2016; Scheiber et al., 2019). The concept of BSF can thus be very useful when characterising complex faults, because BSF can help resolve the spatial and temporal deformation history of fault zones in multiply deformed bedrock

terranes, which have experienced both ductile and brittle deformation. Additionally, BSF can be an important tool to investigate and constrain in time the diachronic and heterogeneous evolution of fault cores.

Acknowledgments

This paper presents some of the results obtained during the BASE project ("Basement fracturing and weathering onshore and offshore Norway—Genesis, age, and landscape development"), a research initiative launched and steered by the Geological Survey of Norway (NGU) and funded by Det Norske Oljeselskap (now Aker BP ASA), Lundin Petroleum, Maersk Oil, Wintershall, and the NGU. The paper finalisation took place during the BASE 2 project supported by Equinor, Aker BP, NPD, Lundin, Spirit Energy, Wintershall and NGU. TEM work was carried out using the NORTEM infrastructure at the TEM Gemini Centre of the Norwegian University of Science and Technology (NTNU), Norway. Ruikai Xie at the Geological Survey of Norway is thanked for performing K analyses. We thank all BASE colleagues for continuous discussion and constructive inputs. Laurel Goodwin and an anonymous reviewer are thanked for having greatly improved the initial version of this paper.

Figure 1: a) Simplified geological map of southwestern Norway with the main structural features of the area. Black star: Lærdal study site; b) Schmidt projection (lower hemisphere) of the principal and secondary slip surfaces of the fault and their associated striae. The black arrows show the direction of slip of the hanging wall; c) detailed view to the southwest of the studied LGF outcrop. The principal slip surface (red dashed line) is represented by a thin, laterally continuous smear of dark gouge, while two subparallel secondary slip surfaces (yellow dashed lines) frame the fault core. Stars indicate sample

locations. All samples were dated by K-Ar. A 40 cm long hammer for scale in the lower part of the outcrop; d) simplified scheme of the BSF of the fault core.

Figure 2: Structural features of the LGF. a) Cm-thick epidote and quartz vein cutting across the hanging wall monzogranite; b) upper secondary slip surface. The red lines represent the direction of slip of the missing block, i.e., the footwall, according to the slickenlines; c) white sigmoidal lenses of cataclasite embedded by the pale green cataclasite (BSF II) constraining a top-to-the-NW sense of shear; d) top-to-the-NW sigmoidal lens of dark reddish grey indurated gouge (BSF I) embedded within a weakly foliated gouge (BSF III); e) extensional top-to-the-NW bookshelf structures within dark competent reddish grey gouge (BSF I); f) lens of dark reddish grey indurated gouge (BSF I) cut by Riedel fractures. Both the reddish gouge and the host fault rock contain white, undulate zeolite veins subparallel to the principal slip surface, marked by yellow arrows.

Figure 3: Different brittle structural facies of the fault core and their representative samples for K-Ar dating. The colours of the labels from "a" to "e" are the same of Fig. 2. a) BSF I, lens of dark reddish grey indurated gouge; b) BSF II, pale green cataclastic brittle domain representing the most common portion of the fault core; c) BSF III, green, weakly foliated gouge embedding a lithon of BSF I; d) BSF IV, clay-rich gouge preserved just below the principal slip surface of "e" and "f"; e) BSF V, dark smear of black gouge representing a laterally continuous, only a few mm-thick layer along the principal slip surface (f).

Figure 4: Microphotographs of representative microstructures of the main LGF fault rocks. a) View of thin section cut perpendicular to the foliation and parallel to the stretching lineation. Mylonitic gneiss from the hanging wall of the LGF with quartz-feldspar domains within an epidote and chlorite-defined foliation. A feldspar sigmoidal lens indicates simple shear deformation; b) cataclasite, enriched in epidote, resulting from the hanging wall protolith; note widespread fracturing and the presence of poorly sorted, angular clasts; c-h)

views of thin sections cut perpendicular to the fault and parallel to slickenlines; c) SEM image of clasts (in yellow) of spherulites (in white) in a fault gouge matrix, representing heavily transposed and recrystallised pseudotachylyte fragments; d) SEM image of clasts of different fault rock domains and mylonites (in yellow) embedded within an ultracataclastic matrix within the pale green cataclasite (BSF II); e) microphotograph of the same ultracataclastic matrix of (d) with flow structures; f) SEM image of a gouge clast in BSF II made of feldspars, smectite, quartz and oxides. The clast is cut by Fe-chlorite and K-feldspar veins; g) laumontite crystals around clasts of an early generation of indurated fault gouge; h) fibrous calcite veins parallel to the NW-SE striae. Mineral abbreviations after Whitney and Evans (2010).

Figure 5: Mineralogical composition of each BSF. a-d) Photos and EDS spectra of K-bearing phases in the <0.1 μm fraction by TEM analysis; e) XRD compositional data for each of the studied fractions.

Figure 6: K-Ar age vs. grain size diagram, showing inclined age curves for all samples. A mean age of c. 179 ± 2 Ma is computed for the two coarsest fractions of all samples, highlighted by the light blue bar.

Figure 7: Conceptual model of LGF evolution through time. a) Pseudotachylyte formed during coseismic rupturing, and an earlier fault zone formed at the expense of a mylonitic shear zone. Fluid infiltration created a network of epidote and quartz veins; b) deformation and fluid ingress led to the formation of a dark reddish grey, indurated gouge and caused overall strengthening of the fault core. The gouge embeds clasts of pseudotachylyte; a fracture-rich damage zone (DZ) formed; c) renewed cataclasis affected the previously formed BSF and the host rock leading to the widening of the active fault zone and the formation of the pale green cataclastic facies in the Late Cretaceous; d) at c. 87 Ma a weakly foliated gouge developed in the inner part of the fault core, leading to the

progressive narrowing of the active zone; e) extreme localisation led to the formation of a green-grey gouge highly enriched in clay minerals; f) a thin, laterally continuous smear of dark gouge cut across all the other BSF, accommodating a last transtensional top-to-the-W increment of faulting at c. 57 Ma.

Table 1: XRD data. Mineral concentrations are given in wt%. GOF represents "Goodness of Fit". "x": unquantified amount.

Sample	Size fraction [µm]	Quartz	K-feldspar	Plagioclase	Illite/ Muscovite	Chlorite	Smectite	Stilbite	Laumontite	Heulandite	Epidote	Pyroxene	Calcite	GOF
BSF I	0.1-0.4	-	30	-	-	32	26	-	2	-	4	6	trace?	1.76
	0.4-2	-	40	-	-	27	18	-	2	-	7	6	trace?	1.51
	2-6	-	47	-	-	23	13	-	2	-	10	5	trace?	1.47
	6-10	-	50	trace	-	22	12	-	2	-	9	4	1	1.43
BSF II	0.4-2	-	12	30	trace?	20	8	4	6	trace	16	4	-	1.51
	2-6	-	11	26	-	10	5	8	17	trace	20	3	-	1.46
	6-10	-	10	24	-	8	4	12	21	trace	18	3	-	1.47
BSF III	<0.1	<0.1	-	-	-	x?	x	x	-	-		x	x	-
	0.1-0.4	-	9	10	-	36	22	-	trace	-	18	5	-	1.65
	0.4-2	trace	9	17	-	15	11	-	trace	-	43	4	1	1.43
	2-6	1	9	17	-	12	9	-	2	-	45	4	1	1.41
	6-10	1	10	20	-	12	8	-	2	-	42	3	2	1.38
BSF IV	<0.1	-	x	-	x	x	x	-	-	-	x	-	-	-
	0.1-0.4	2	22	-	14	21	29	-	-	-	8	-	3	1.56
	0.4-2	4	33	-	15	13	20	-	-	-	13	-	2	1.42
	2-6	11	37	-	5	11	16	-	-	-	19	-	1	1.37
	6-10	14	35	-	4	11	15	-	-	-	19	-	2	1.35
BSF V	0.1-0.4	-	27	4	30	21	14	-	-	-	4	-	-	1.4
	0.4-2	-	25	5	30	20	15	-	-	-	5	-	-	1.4
	2-6	6	38	6	8	8	5	1	trace	-	28	-	-	1.34
	6-10	7	39	5	5	9	7	1	2	-	25	-	-	1.35

Table 2: K-Ar radiometric data and ages for each grain size fraction of the samples.

Sample Parameters			^{40}Ar*			K		Age Data	
Sample	Size fraction [µm]	Mass [mg]	^{40}Ar* [mol/g]	σ [%]	^{40}Ar* [%]	K [wt %]	σ [%]	Age [Ma]	σ [Ma]
BSF I	<0.1	0.72	2.73E-10	0.99	62.1	1.261	2.00	120.8	2.7
	0.1-0.4	2.50	6.58E-10	0.34	87.8	2.452	2.00	148.5	3.0
	0.4-2	3.25	1.18E-09	0.31	92.5	3.877	2.00	168.1	3.4
	4-6	4.36	1.58E-09	0.30	97.8	4.685	2.00	184.8	3.7
	6-10	3.73	1.76E-09	0.31	98.5	5.171	2.00	186.3	3.8
BSF II	0.1-0.4	1.92	2.44E-10	0.48	93.6	1.028	2.00	132.0	2.7
	0.4-2	2.23	3.95E-10	0.38	78.4	1.356	2.00	160.7	3.3
	4-6	7.56	4.51E-10	0.29	96.3	1.324	2.00	186.4	3.8
	6-10	8.72	4.46E-10	0.29	93.9	1.250	2.00	194.9	3.9
BSF III	<0.1	2.23	4.89E-11	1.44	18.4	0.318	2.00	86.6	2.1
	0.1-0.4	3.69	1.66E-10	0.39	59.2	0.789	2.00	117.7	2.4
	0.4-2	3.30	2.77E-10	0.35	80.6	1.029	2.00	148.8	3.0
	4-6	2.04	3.45E-10	0.40	86.1	1.031	2.00	183.2	3.7
	6-10	3.39	3.39E-10	0.34	91.2	1.119	2.00	166.8	3.4
BSF IV	<0.1	1.32	1.14E-10	1.07	20.2	0.830	2.00	77.7	1.8
	0.1-0.4	3.13	3.2E-10	0.35	57.0	1.543	2.00	115.8	2.4
	0.4-2	3.23	9.09E-10	0.31	81.4	3.071	2.00	163.0	3.3
	4-6	5.61	1.29E-09	0.29	93.6	3.927	2.00	179.8	3.6
	6-10	3.46	1.28E-09	0.31	92.1	3.793	2.00	184.3	3.7
BSF V	<0.1	1.32	1.29E-10	0.96	49.4	1.278	2.00	57.4	1.3
	0.1-0.4	1.70	4.32E-10	0.42	78.3	2.639	2.00	91.9	1.9
	0.4-2	1.79	9.99E-10	0.37	91.5	3.983	2.00	139.1	2.8

4-6	4.73	1.28E-09	0.30	97.5	4.034	2.00	174.1	3.5
6-10	2.62	1.26E-09	0.33	96.4	4.115	2.00	168.7	3.4

Aldega, L., Viola, G., Casas-Sainz, A., Marcén, M., Román-Berdiel, T., Lelij, R., 2019. Unravelling multiple thermo-tectonic events accommodated by crustal-scale faults in northern Iberia, Spain: Insights from K-Ar dating of clay gouges. Tectonics https://doi.org./10.1029/2019tc005585.

Andersen, T.B., Torsvik, T.H., Eide, A.E., Osmundsen, P.T., Faleide, J.I., 1999. Mesozoic extensional faulting within the Caledonides of central south Norway. J. Geol. Soc. 156, 1073-1080,

Aydin, A., 2000. Fractures, faults, and hydrocarbon entrapment, migration and flow. Marine and Petroleum Geology 17, 797-814,

Bense, F.A., Wemmer, K., Loebens, S., Siegesmund, S., 2013. Fault gouge analyses: K-Ar illite dating, clay mineralogy and tectonic significance - A study from the Sierras Pampeanas, Argentina. Int. J. Earth Sci. https://doi.org./10.1007/s00531-013-0956-7.

Braathen, A., Tveranger, J., Fossen, H., Skar, T., Cardozo, N., Sernshaug, S.E., Bastesen, E., Sverdrup, E., 2009. Fault facies and its application to sandstone reservoirs. Aapg Bull. 93, 891-917, https://doi.org./10.1306/03230908116.

Brockamp, O., Clauer, N., 2013. Hydrothermal and unexpected diagenetic alteration in Permian shales of the Lodève epigenetic U-deposit of southern France, traced by K–Ar illite and K-feldspar dating. Chem. Geol. 357, 18-28, https://doi.org./10.1016/j.chemgeo.2013.08.009.

Caine, J.S., Evans, J.P., Forster, C.B., 1996. Fault zone architecture and permeability structure. Geology 24, 1025-1028,

Chester, F.M., Logan, J.M., 1986. Implications for Mechanical Properties of Brittle Faults from Observations of the Punchbowl Fault Zone, California. Pure Appl. Geophys. 124, 79–106,

Clauer, N., 2013. The K-Ar and 40Ar/39Ar methods revisited for dating fine-grained K-bearing clay minerals. Chem. Geol. 354, 163-185, https://doi.org./10.1016/j.chemgeo.2013.05.030.

Corfu, F., Andersen, T.B., Gasser, D., 2014. The Scandinavian Caledonides: main features, conceptual advances and critical questions. Geol. Soc. London, Spec. Publ. 390, 9-43, https://doi.org./10.1144/sp390.25.

Davids, K., Wemmer, K., Zwingmann, H., Kohlmann, F., Jacobs, J., Bergh, S.G., 2013. K–Ar illite and apatite fission track constraints on brittle faulting and the evolution of the northern Norwegian passive margin. Tectonophysics 608, 196-211, https://doi.org./10.1016/j.tecto.2013.09.035.

Di Toro, G., Pennacchioni, G., 2004. Superheated friction-induced melts in zoned pseudotachylytes within the Adamello tonalites (Italian Southern Alps). J. Struct. Geol. 26, 1783-1801, https://doi.org./10.1016/j.jsg.2004.03.001.

Evans, J.P., Forster, C.B., Goddard, J.V., 1997. Permeability of fault-related rocks, and implications for hydraulic structure of fault zones. Journal of Structural Geology, 19, 1393-1404,

Faulkner, D.R., Rutter, E.H., 2003. The effect of temperature, the nature of the pore fluid, and subyield differential stress on the permeability of phyllosilicate-rich fault gouge. Journal of Geophysical Research: Solid Earth 108 https://doi.org./10.1029/2001jb001581.

Ferrill, D.A., Morris, A.P., Evans, M.A., Burkhard, M., Groshong, R.H., Onasch, C.M., 2004. Calcite twin morphology: a low-temperature deformation geothermometer. J. Struct. Geol. 26, 1521-1529, https://doi.org./10.1016/j.jsg.2003.11.028.

Fossen, H., Dunlap, W.J., 1998. Timing and kinematics of Caledonian thrusting and extensional collapse, southern Norway: Evidence from $^{40}Ar/^{39}Ar$ thermochronology. J. Struct. Geol. 20, 765-781,

Fossen, H., Hurich, C.A., 2005. The Hardangerfjord Shear Zone in SW Norway and the North Sea: a large-scale low-angle shear zone in the Caledonian crust. J. Geol. Soc. London 162, 675-687, https://doi.org./10.1144/0016-764904-136.

Fossen, H., Khani, H.F., Faleide, J.I., Ksienzyk, A.K., Dunlap, W.J., 2016. Post-Caledonian extension in the West Norway–northern North Sea region: the role of structural inheritance. Geol. Soc. London, Spec. Publ. 439, 465-486, https://doi.org./10.1144/sp439.6.

Gabrielsen, R.H., Odinsen, T., Grunnaleite, I., 1999. Structuring of the Northern Viking Graben and the More Basin; the influence of basement structural grain and the particular role of the More Trondelag Fault Complex. Marine and Petroleum Geology 16, 443-465,

Haines, S.H., van der Pluijm, B.A., 2008. Clay quantification and Ar-Ar dating of synthetic and natural gouge: Application to the Miocene Sierra Mazatan detachment fault, Sonora, Mexico. J. Struct. Geol. 30 https://doi.org./10.1016/j.jsg.2007.11.012.

Holdsworth, R.E., 2004. Weak faults - Rotten cores. Science 303, 181-182,

Johannessen, K.C., Kohlmann, F., Ksienzyk, A.K., Dunkl, I., Jacobs, J., 2013. Tectonic evolution of the SW Norwegian passive margin based on low-temperature thermochronology from the innermost Hardangerfjord area. Norw. J. Geol. 93, 243-260,

Kelley, S.P., 2002. Excess argon in K–Ar and Ar–Ar geochronology. Chem. Geol. 188, 1-22,

Ksienzyk, A.K., Dunkl, I., Jacobs, J., Fossen, H., Kohlmann, F., 2014. From orogen to passive margin: constraints from fission track and (U-Th)/He analyses on Mesozoic uplift and fault reactivation in SW Norway., Geol. Soc. London Spec. Publ.

Ksienzyk, A.K., Wemmer, K., Jacobs, J., Fossen, H., Schomberg, A.C., Süssenberger, A., Lünsdorf, N.K., Bastesen, E., 2016. Post-Caledonian brittle deformation in the Bergen area. Norw. J. Geol. 96 https://doi.org./10.17850/njg96-3-06.

Lin, A., 1994. Microlite Morphology and Chemistry in Pseudotachylite, from the Fuyun Fault Zone, China. The Journal of Geology 102, 317-329,

Mark, D.F., Kelley, S.P., Lee, M.R., Parnell, J., Sherlock, S.C., Brown, D.J., 2008. Ar-Ar dating of authigenic K-feldspar: Quantitative modelling of radiogenic argon-loss through subgrain boundary networks. Geochim. Cosmochim. Ac. 72, 2695-2710, https://doi.org./10.1016/j.gca.2008.03.018.

Milnes, A.G., Corfu, F., 2011. Structural Geology and Tectonic Evolution of the Sognefjord Transect, Caledonian Orogen, Southern Norway—A Field Trip Guide. Geol. Soc. Am. Field Guide 19 https://doi.org./10.1130/2011.0019.

Olsen, M.P., Scholz, C.H., Léger, A., 1998. Healing and sealing of a simulated fault gouge under hydrothermal conditions: Implications for fault healing. J. Geoph. Res. 103, 7421-7430,

Pevear, D.R., 1999. Illite and hydrocarbon exploration. P. Nat. Acad. Sci. USA 96, 3440-3446,

Pleuger, J., Mancktelow, N., Zwingmann, H., Manser, M., 2012. K–Ar dating of synkinematic clay gouges from Neoalpine faults of the Central, Western and Eastern Alps. Tectonophysics 550-553, 1-16, https://doi.org./10.1016/j.tecto.2012.05.001.

Rutter, E.H., Holdsworth, R.E., Knipe, R.J., 2001. The nature and tectonic significance of fault-zone weakening: an introduction. Geol. Soc. London, Spec. Publ. 186, 1-11,

Sasseville, C., Tremblay, A., Clauer, N., Liewig, N., 2008. K–Ar age constraints on the evolution of polydeformed fold–thrust belts: The case of the Northern Appalachians (southern Quebec). J. Geodyn. 45, 99-119, https://doi.org./10.1016/j.jog.2007.07.004.

Scheiber, T., Viola, G., 2018. Complex Bedrock Fracture Patterns: A Multipronged Approach to Resolve Their Evolution in Space and Time. Tectonics 37, 1030-1062, https://doi.org./10.1002/2017tc004763.

Scheiber, T., Viola, G., van der Lelij, R., Margreth, A., Schönenberger, J., 2019. Microstructurally-constrained versus bulk fault gouge K-Ar dating. J. Struct. Geol. 127 https://doi.org./10.1016/j.jsg.2019.103868.

Surace, I.R., Clauer, N., Thélin, P., Pfeifer, H.R., 2011. Structural analysis, clay mineralogy and K–Ar dating of fault gouges from Centovalli Line (Central Alps) for reconstruction of their recent activity. Tectonophysics 510, 80-93, https://doi.org./10.1016/j.tecto.2011.06.019.

Tagami, T., 2012. Thermochronological investigation of fault zones. Tectonophysics 538, 67-85, https://doi.org./10.1016/j.tecto.2012.01.032.

Torgersen, E., Viola, G., Zwingmann, H., Harris, C., 2015a. Structural and temporal evolution of a reactivated brittle-ductile fault - Part II: Timing of fault initiation and reactivation by K-Ar dating of synkinematic illite/muscovite. Earth Planet. Sc. Lett. 410, 212-224, https://doi.org./10.1016/j.epsl.2014.11.013.

Torgersen, E., Viola, G., Zwingmann, H., Henderson, I.H.C., 2015b. Inclined K-Ar illite age spectra in brittle fault gouges: effects of fault reactivation and wall-rock contamination. Terra Nova 27, 106-113, https://doi.org./10.1111/ter.12136.

van der Pluijm, B.A., Hall, C.M., Vrolijk, P.J., Pevear, D.R., Covey, M.C., 2001. The dating of shallow faults in the Earth's crust. Nature 412, 172-174,

Verdel, C., van der Pluijm, B.A., Niemi, N., 2012. Variation of illite/muscovite 40 Ar/39 Ar age spectra during progressive low-grade metamorphism: an example from the US Cordillera. Contrib. Mineral. Petr. 164, 521-536, https://doi.org./10.1007/s00410-012-0751-7.

Viola, G., Scheiber, T., Fredin, O., Zwingmann, H., Margreth, A., Knies, J., 2016. Deconvoluting complex structural histories archived in brittle fault zones. Nat. Commun. 7, 13448, https://doi.org./10.1038/ncomms13448.

Viola, G., Torgersen, E., Mazzarini, F., Musumeci, G., van der Lelij, R., Schönenberger, J., Garofalo, P.S., 2018. New Constraints on the Evolution of the Inner Northern Apennines by K-Ar Dating of Late Miocene-Early Pliocene Compression on the Island of Elba, Italy. Tectonics https://doi.org./10.1029/2018tc005182.

Viola, G., Zwingmann, H., Mattila, J., Kapyaho, A., 2013. K-Ar illite age constraints on the Proterozoic formation and reactivation history of a brittle fault in Fennoscandia. Terra Nova 25, 236-244, https://doi.org./10.1111/ter.12031.

Vrolijk, P., Pevear, D., Covey, M., LaRiviere, A., 2018. Fault gouge dating: history and evolution. Clay Minerals 53, 305-324, https://doi.org./10.1180/clm.2018.22.

Walsh, E.O., Hacker, B.R., Gans, P.B., Wong, M.S., Andersen, T.B., 2013. Crustal exhumation of the Western Gneiss Region UHP terrane, Norway: 40Ar/39Ar thermochronology and fault-slip analysis. Tectonophysics 608, 1159-1179, https://doi.org./10.1016/j.tecto.2013.06.030.

Weisenberger, T., Bucher, K., 2010. Zeolites in fissures of granites and gneisses of the Central Alps. J. Metamorph. Geol. 28, 825-847, https://doi.org./10.1111/j.1525-1314.2010.00895.x.

Whitney, D.L., Evans, B.W., 2010. Abbreviations for names of rock-forming minerals. Am. Miner. 95, 185-187, https://doi.org./10.2138/am.2010.3371.

Yamasaki, S., Zwingmann, H., Yamada, K., Tagami, T., Umeda, K., 2013. Constraining the timing of brittle deformation and faulting in the Toki granite, central Japan. Chem. Geol. 351, 168-174, https://doi.org./10.1016/j.chemgeo.2013.05.005.

Zwingmann, H., Mancktelow, N., 2004. Timing of Alpine fault gouges. Earth Planet. Sc. Lett. 223, 415-425, https://doi.org./10.1016/j.epsl.2004.04.041.

Appendix

The mineralogical composition of all grain size fractions was studied with X-ray diffraction (XRD). Randomly-oriented samples were prepared by side-loading and analysed with a Bruker D8 Advance X-ray diffractometer operating with a Cu X-ray tube (40 kV/40 mA) and Lynxeye XE detector. XRD scanning was performed from 3 to 75° 2θ with a step size of 0.02° 2θ, a measurement time of 1 s per step, and rotation speed of 30° per minute. Fixed divergence had an opening of 0.6 mm and primary and secondary soller slits were 2.5°. A knife edge was used to reduce scatter radiation. Mineral identification was carried out with the automatic and/or manual peak search-match function of Bruker's Diffrac.EVA V4.2 software using both Crystallographic Open Database (COD) as well as the PDF 4 Minerals database from the International Centre for Diffraction Data (ICDD). For further clay minerals study, oriented mounts of fractions 2-6 µm were prepared by letting 1 ml of sample suspension dry out on a glass slide. These slides were measured from 2 to 40° 2θ at room temperature, after treatment with ethylene glycol for 24 h, and after heating at 550 °C for 1 h

The procedure followed to perform K-Ar dating of each grain size fractions starts with packing aliquots of air-dry clay samples in molybdenum foil. They are weighed using a Mettler Toledo XPE26DR microbalance, with a resolution of 2 µg and a combined weighing uncertainty of 4 µg. Samples are degassed at 1400 °C for 10 minutes. The

evolved gas is spiked with a known amount of isotopically pure ^{38}Ar and purified in two stages with a Titanium Sublimation Pump and a combination of two SAES GP50 ST101 getters, one at 300 °C and one at 22 °C. The purified argon is analysed in static vacuum in an IsotopX NGX multicollector noble gas mass spectrometer using faraday cups with 1012Ω amplifiers for ^{38}Ar and ^{36}Ar and a 1111Ω amplifier for ^{40}Ar; the gas is analysed for 600 integrations of 1 second. Baseline corrected volts are regressed back to inlet time using an exponential best fit regression function. Blanks are run periodically. Mass bias corrections are performed using a power law on blank corrected intercept values by using within-batch air analyses compared with the atmospheric $^{40}Ar/^{36}Ar$ composition of 298.56 ± 0.31 (Lee et al., 2006). The ^{38}Ar spike is calibrated using HD-B1 biotite (Fuhrmann et al., 1987) with a $^{40}Ar^*$ concentration of 3.351x10-11mol/g (Charbit et al., 1998). Long term reproducibility of many aliquots of HD-B1 biotite is better than 0.3% RSD.

Potassium concentrations are determined by fluxing approximately 50 mg of clay sample in lithium tetraborate. The resulting glass is dissolved in HNO_3 spiked with a known concentration of Rh as internal standard. The K concentration is analysed using a Perkin Elmer Optima 4300DV ICP-OES. The uncertainty of K determination is estimated from evaluating the accuracy of several whole rock standards with similar K concentration range and is better than 2%.

Radiogenic 40Ar* concentrations, relative uncertainties, and K-Ar ages are calculated using the equation of Hałas and Wójtowicz (2014), using the decay constants of Renne et al. (2011).

Charbit, S., Guillou, H. and Turpin, L., 1998. Cross calibration of K–Ar standard minerals using an unspiked Ar measurement technique. Chem. Geol. 150(1-2), 147-159.

Fuhrmann, U., Lippolt, H. and Hess, J.C., 1987. HD-B1 biotite reference material for K-Ar chronometry. Chem. Geol. 66, 41-51.

Hałas, S., Wójtowicz, A., 2014. Propagation of error formulas for K/Ar dating method. Geochronometria 41, 202-206. https://doi.org/10.2478/s13386-013-0162-1

Lee, J.Y., Marti, K., Severinghaus, J.P., Kawamura, K., Yoo, H.S., Lee, J.B. and Kim, J.S., 2006. A redetermination of the isotopic abundances of atmospheric Ar. Geochim. Cosmochim. Ac. 70, 4507-4512. https://doi.org/10.1016/j.gca.2006.06.1563

Renne, P.R., Balco, G., Ludwig, K.R., Mundil, R., Min, K., 2011. Response to the comment by W.H. Schwarz et al. on “Joint determination of 40K decay constants and 40Ar∗/40K for the Fish Canyon sanidine standard, and improved accuracy for 40Ar/39Ar geochronology” by P.R. Renne et al. (2010). Geochim. Cosmochim. Ac. 75, 5097-5100. https://doi.org/10.1016/j.gca.2011.06.021

Figure1
Click here to download Figure: Figure1.pdf

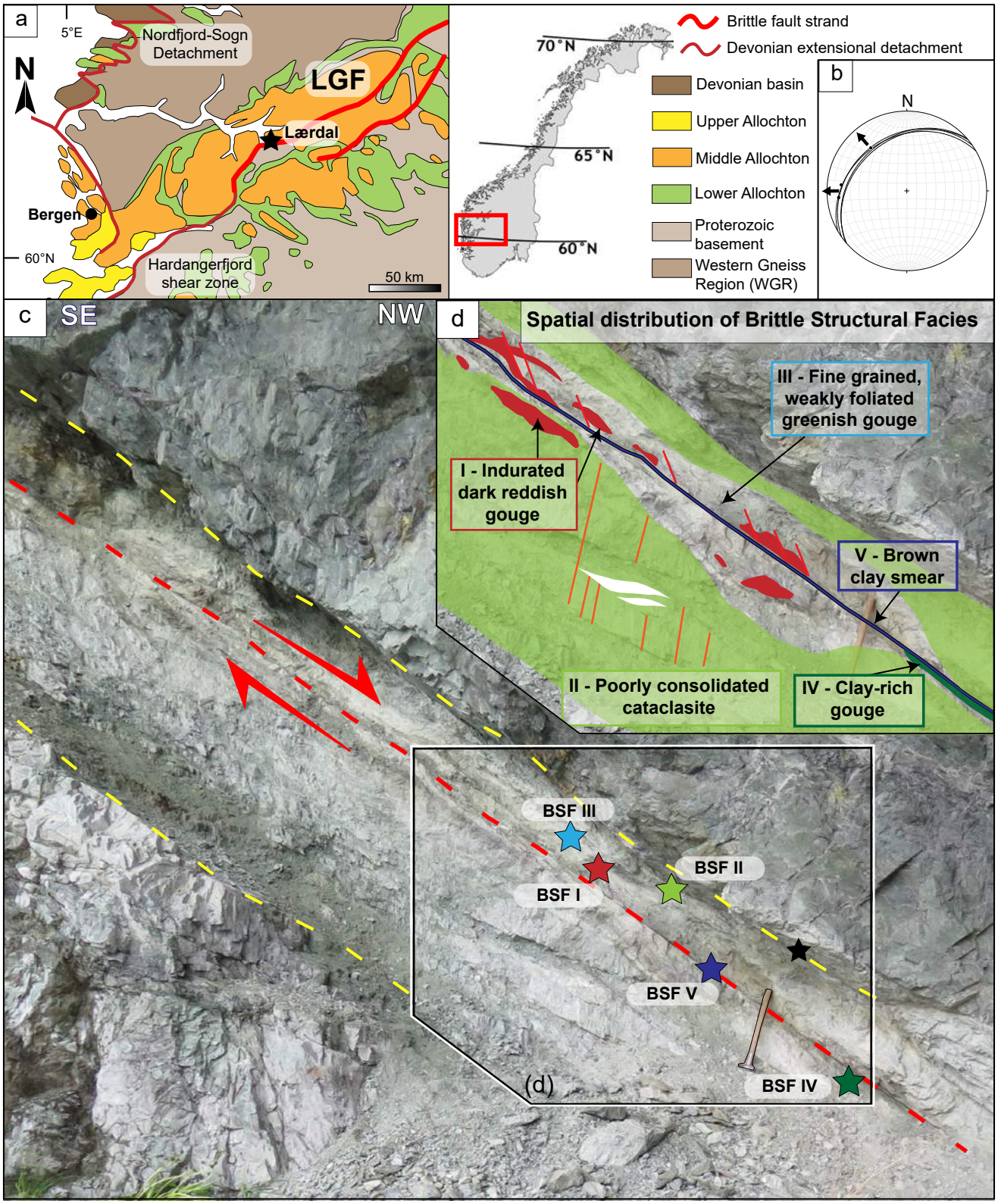

Figure2

Click here to download Figure: Figure2.pdf

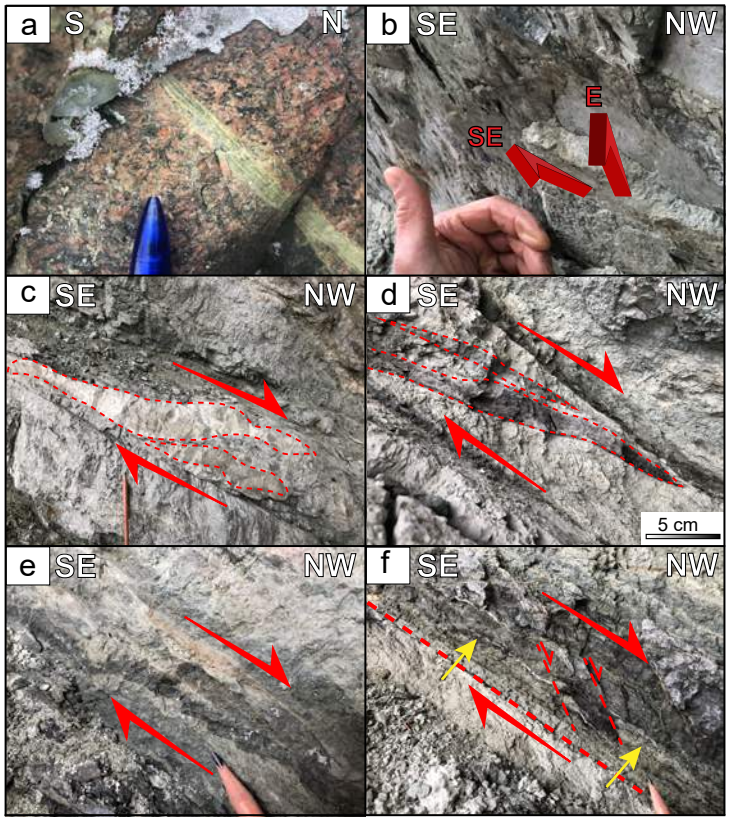

Figure3

Click here to download Figure: Figure3.pdf

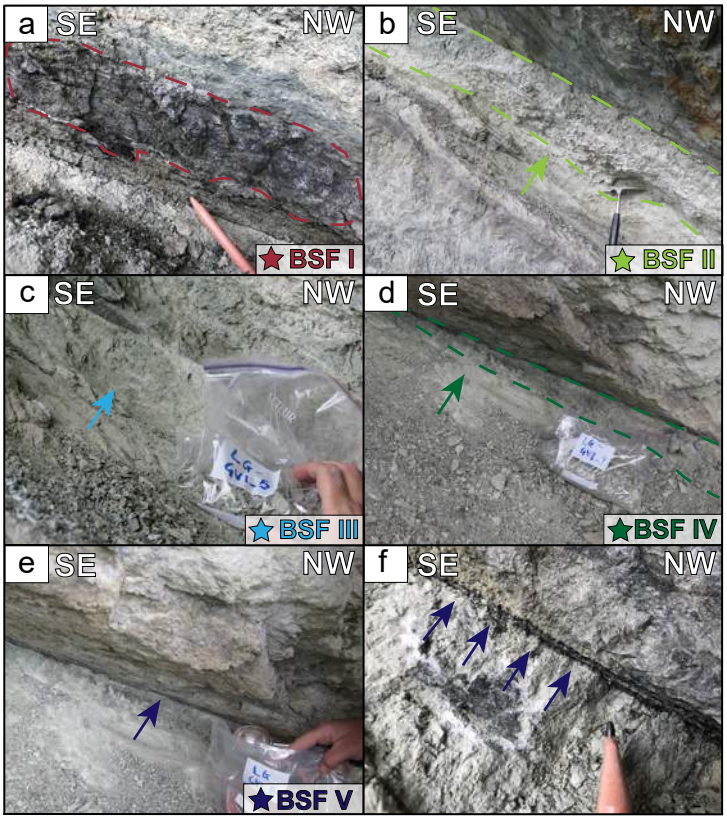

Figure4

Click here to download Figure: Figure4.pdf

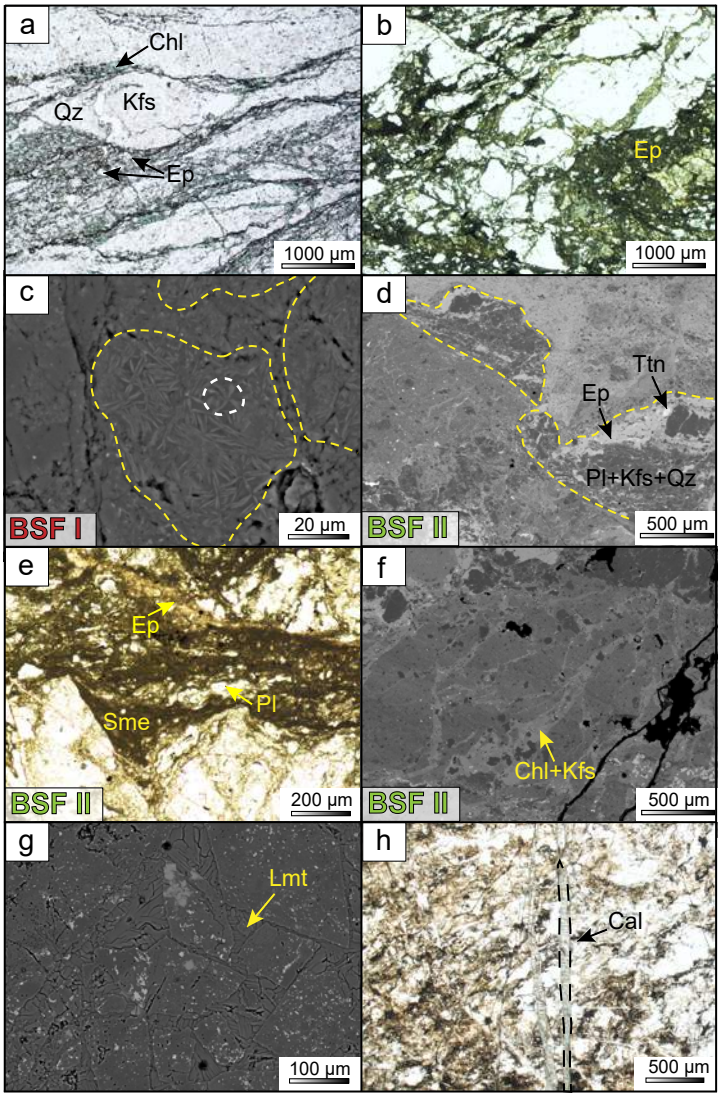

Figure5

Click here to download Figure: Figure5.pdf

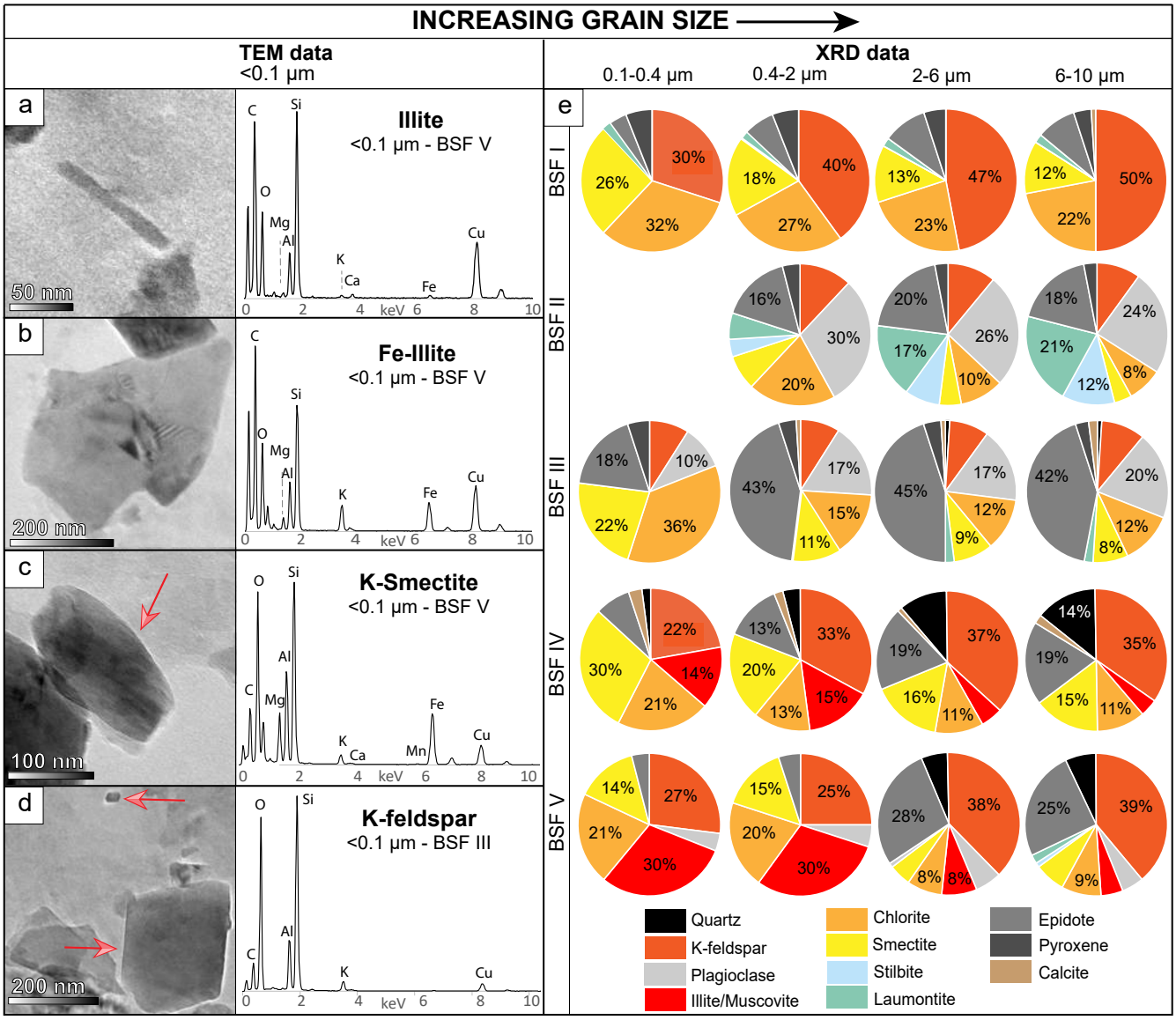

Figure6
Click here to download Figure: Figure6.pdf

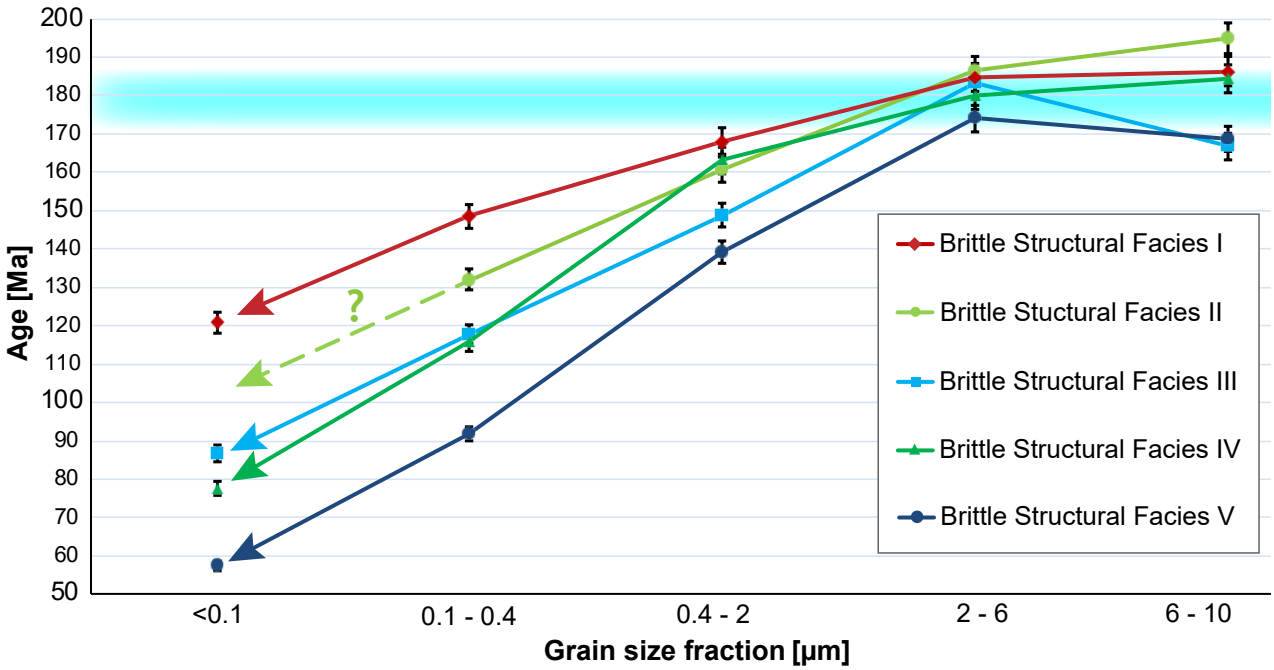

Figure7

Click here to download Figure: Figure7.pdf